Document downloaded from:

http://hdl.handle.net/10251/141652

This paper must be cited as:

Tanov, S.; Pachano-Prieto, LM.; Andersson, Ö.; Wang, Z.; Richter, M.; Pastor, JV.; García-Oliver, JM.... (01-2). Influence of spatial and temporal distribution of Turbulent Kinetic Energy on heat transfer coefficient in a light duty CI engine operating with Partially Premixed Combustion. Applied Thermal Engineering. 129:31-40. https://doi.org/10.1016/j.applthermaleng.2017.10.006

The final publication is available at

https://doi.org/10.1016/j.applthermaleng.2017.10.006

Copyright Elsevier

Additional Information

Influence of Spatial and Temporal Distribution of Turbulent Kinetic Energy on Heat Transfer Coefficient in a Light Duty CI Engine Operating with Partially Premixed Combustion

Authors:

Slavey Tanov[1], Leonardo Pachano[2], Öivind Andersson[1], Zhenkan Wang[3], Mattias Richter[3], José V. Pastor[2], José M. García-Oliver[2], Antonio García[2]

Affiliation:

1. Division of Combustion Engines, Lund University, Sweden
2. CMT Motores Térmicos – Universitat Politècnica de València, Camino de Vera s/n, 46022, Valencia, Spain.
3. Division of Combustion Physics, Lund University, Sweden

Corresponding author

Dr. Antonio García

CMT - Motores Térmicos /Universitat Politècnica de València

angarma8@mot.upv.es

Abstract

Emission regulations together with the need of more fuel-efficient engines have driven the development of promising combustion concepts in compression ignition (CI) engines. Most of these combustion concepts, lead toward a lean and low temperature combustion potentially suitable to achieve lower emission and fuel consumption levels compared to conventional diesel combustion. In this framework, Partially Premixed Combustion (PPC) using gasoline as fuel is one of the most accepted concepts. There are numerous studies focused on studying concepts such as PPC from the emissions point of view. Nonetheless, there is a lack of knowledge regarding changes in heat transfer introduced by the use of these combustion concepts. It is worth noting that heat transfer can be considered as a key aspect behind possible engine performance improvements. Thus, the reliable estimation of this parameter is of considerable importance. Additionally, a better understanding of how events such as injection and combustion might affect heat transfer is also relevant.

To gain insight into gasoline PPC heat transfer coefficient, its evolution during late compression and early expansion were studied. In particular, this work aims to analyze Turbulent Kinetic Energy (TKE) spatial and temporal evolution influence on heat transfer coefficient. The analysis is based on experimental TKE maps derived from Particle Image Velocimetry (PIV) data. For the heat transfer coefficient estimation a modified Woschni correlation has been used. Results from several injection strategies and a reference motored case have been analyzed. It has been found that injection strategy has a considerable influence on the TKE field and hence on heat transfer coefficient evolution.

1 Introduction

Low Temperature Combustion (LTC) technologies, like Homogenous Charge Compression Ignition (HCCI) [1–3], Partially Premixed Combustion (PPC) [4,5] and Reactivity Controlled Compression Ignition (RCCI) [6–9] have been widely studied in the last decade because they are expected to achieve low engine-out emissions along with high thermal efficiency. In this context, gasoline PPC has received increasingly attention due to its potential for simultaneously reducing fuel consumption and NOx emissions in gasoline Spark Ignition (SI) engines, and its capability to avoid soot and NOx emissions in CI diesel engines. Several experimental and numerical investigations of this combustion type have been performed over the recent years. PPC is achieved by controlling the injection events, inlet temperature and pressure, and composition of the fuel-air mixture, so that it ignites close to Top Dead Center (TDC). It is

similar in nature to HCCI, with significantly early fuel injection in the cycle and a combustion process that occurs as a sequence of auto-ignition events. The main difference between HCCI and PPC is that the goal of PPC is to control auto-ignition timing with moderately early fuel injections (~20 CAD bTDC) by manipulating the in-cylinder charge stratification level.

PPC is highly dependent on the level of in-cylinder fuel stratification at the start of combustion (SOC). Recent work performed by Izadi et al [10] focused on investigation of combustion stratification using single injections. They concluded that combustion stratification is low and almost independent of start of injection (SOI) for early injections, while there is a remarkable reverse correlation between combustion timing and stratification level for the late injections (-45 to -12.5 CAD). Lee and Reitz [11] investigated characteristics of PCCI with single early injection. Their results demonstrated that combustion performance and emissions are strongly affected by injection timing. They also indicated that spray targeting at the surface of piston bowl directly influenced emissions formation. Spray targeting point, which was located near the edge of piston bowl, was considered as the optimum in PCCI combustion through different engine operating conditions because the squish flow would promote mixture preparation when spray is injected at this location.

Multiple injection strategies with early injection pulses are usually employed to promote different levels of fuel stratification. Early study [12] on combustion stratification using different injection strategies had shown that the combustion following triple injection is more homogeneous compared to single and double injection. Manente et al. [13] employed triple pulse injections to control excessive fuel stratification that causes unacceptable pressure rise rates in a heavy duty diesel engine. They operated the engine at various loads using fixed SOI timings for the three pulses. Kalghatgi et al. [14] tested the effectiveness of triple injection on controlling heat release rates as well as improving engine performance in a small-bore diesel engine fueled with RON84 gasoline. Sellnau et al. [15–17] applied a triple-injection method to improve fuel economy in a light duty (LD) diesel engine operated with RON91 gasoline at 6 bar IMEP. They also showed that a triple injection strategy allowed the use of lower injection pressures compared to single and double-injection strategies.

Studies on multiple injection strategies conducted with experimental fluid dynamics have rarely been reported. The systematic study by the authors [12,18] in the field of experimental fluid dynamics has focused on in-cylinder flow pattern and temporal evolution of turbulence level under PPC conditions.

In view of the potential of PPC and aiming at a more comprehensive study of this combustion mode, the analysis of wall heat transfer coefficient is of particular importance. It has been reported that wall heat transfer affects in-cylinder physical phenomena such as droplet evaporation, auto-ignition and flame-wall interaction [19]. Therefore, wall heat transfer has a deep impact on the overall engine performance. On the one hand, heat losses through cylinder walls reduce energy available to be converted into useful mechanical work affecting indicated efficiency. On the other hand, changes in gas and surface temperature due to heat transfer might also affect pollutant formation [20].

The aim of the current work is to gain insight into heat transfer under PPC operating conditions. To that end, a modified Woschni correlation is used to estimate wall heat transfer coefficient. The modified correlation is not only a function of thermodynamic conditions, but also of the in-cylinder velocity and TKE fields. By using experimental data measured by means of high-speed PIV [12] TKE can be derived from the velocity field. Temporal and spatial TKE distribution and its influence on the heat transfer coefficient is studied. The analysis is carried out for three injection strategies (i.e. single, double and triple injection) as well as for a reference case under motored conditions.

2 Experimental Setup

2.1 Experimental facility

Experiments were performed in a Bowditch-designed single-cylinder engine modified from a Volvo D5 LD diesel engine.

Table 1 shows the engine specifications. Due to the large top ring-land crevice required for side-view imaging, the geometric compression ratio of this optical engine is lower than the target of 16, typical of PPC combustion systems. The engine further allows the intake swirl to be adjusted by a swirl control valve. It was operated at a swirl ratio of 2.6 through this work. A Bosch common rail fuel injection system and a 5-hole solenoid Bosch injector were used for fuel injection.

Engine base type	Volvo D5
Number of cylinders	5
Number of valves	4
Bore	81 mm
Stroke	93.2 mm
Connecting rod	147 mm
Displacement	0.48 L
Compression ratio (metal configuration)	1:16
Compression ratio (optical configuration)	1:11.3
Swirl ratio	2.6
Fuel Injection	
Type	Common Rail
Fuel injector Type	Solenoid
Hydraulic flow	360 cc/30s @ 100 bar
Umbrella angle	140°
Orifice diameter	0.159 mm
Number of holes	5
Hole conicity	1.5

Table 1. Engine and injection system specifications.

2.2 PIV measurement system

An Nd: YLF diode pumped dual cavity laser from Dantec Dynamics (model type: DualPower 30-1000) was used as the light source. Its wavelength is 527 nm and can reach a maximum 30 mJ power per pulse at a running repetition rate of 1 kHz. At 800 rpm engine speed the laser operates at 2.4 kHz with 13 mJ energy per pulse. The light sheet created by the optics unit was aligned with the injector tip installed in the optically accessible engine. The engine is equipped with a production-like optical piston and an optical cylinder liner with height of 25 mm shown in Figure 1. The light sheet was focused in the area between the injector tip and the liner inner surface with a height of around 3 cm through the field of view.

Titanium Dioxide (TiO_2) powder was used as PIV seeding particles, which have a mean particle diameter from 2 to 3 μm and a density of 4260 kg/m^3. Assuming Stokes drag, the particle time constant (τ_s) representing the response time to changes in the flow is roughly 40 μs at TDC-like thermodynamic conditions. At these conditions, τ_s is slightly larger than the estimated Kolmogorov time scale and thus the seeding particles are able to follow most of the turbulent structures. Seeding particles were introduced from a cylindrical container fed by a swirl airflow of around 20 ln/min, which is precisely controlled by a mass flow meter. The seeding flow was

then mixed with the intake stream inside the intake manifold. The TiO_2 powder was baked over 24 hours before seeding it into the engine to efficiently prevent particle agglomeration. In addition, water vapor was added to the intake stream, as part of EGR gases, to reduce the electrostatic charge build-up, and eventually reduce the chance of adhesion of seeding particles to the engine's optical components. These two procedures were proved essential for in-cylinder PIV measurements.

Images were acquired using a Dantec Dynamics high-speed CMOS camera (SpeedSense 710). A Nikkor 105 mm lens with an extension ring (Nikkor PK-13) was also used and the lens aperture was closed as much as possible (f#16) to focus the full field of view. The image format was cropped to 1040x440 pixels to increase the maximum camera frame rate. The exposure time for all image pairs was 63 μs for the first image and around 350 μs for the second image (depending on the engine rotation speed). The long exposure for the second image was due to the time required to readout the first image from camera sensor. The time between the laser pulses was set to 20 μs. According to [21] this time delay between laser pulses is a good compromise between resolving velocity and being able to perform the cross-correlation. The maximum displacement was less than one quarter of the side of the interrogation area as the error increases with increasing displacement [22,23].

Despite the combustion process, TiO_2 powder proved to be a suitable seeding element. Although soot luminosity is known to be a challenge for PIV measurements under reacting conditions, PPC efficiently helps to overcome this issue. No filter was used in these measurements, since little soot luminosity from PPC was observed and thus the Mie scattering light from particles was dominant. The optical piston with a realistic bowl geometry brings significant optical distortion to the acquired image. Considering that the glass piston thickness is irregular in the optical path and that the distortion might depend on the piston position with respect to the camera lens, the distortion is almost impossible to be compensated by adding additional optics between the engine and the camera. Consequently, distortion was handled with a code for image dewarping.

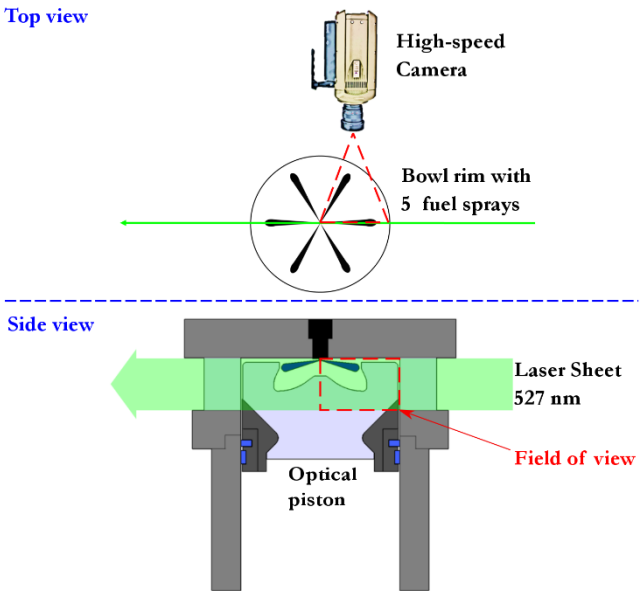

Figure 1. Optical setup.

3 Methodology

3.1 Operating conditions

Throughout this study, the engine was running at 800 rpm, with an injection pressure of 600 bar for 44 continuously fired cycles. A blended fuel, PRF 70, consisting of 30% n-heptane and 70% iso-octane in volume percentage was used for the experiment to achieve suitable ignition delay prior to auto-ignition for PPC. Injection strategy was the main variable for comparison, and three different injection patterns (single, double and triple injection) were investigated. In these experiments the engine load was kept constant at 4 bar IMEP. At SOC, the fuel-air mixture was stratified enough to achieve stable ignition and controlled heat release. The inlet air temperature was kept at 73 °C and the intake air pressure was 1.14 bar (absolute). The experiments were performed in a randomized order after the engine reached a steady thermal state, which corresponded to a cooling water temperature of 65 °C. The exhaust of an industrial fuel-oil burner was used to decrease the oxygen level of the intake charge to 17%. The operating conditions are summarized in

Table 2, while heat release rate and pressure traces for each of the injection strategies proposed are shown in Figure 2.

Engine parameters		
Intake pressure	1.14 bar	
Intake temperature	73 °C ±2 °C	
Injection pressure	600bar ±2 bar	
Swirl ratio	2.6	
O_2	17 vol %	
λ	1.75	
Cooling water temperature	65 °C ±2 °C	
Liner wall temperature	80 °C	
Fuel type	PRF 70	
Seeding particles	TiO_2	
Injection timing	SOI [CAD]	Duration [CAD]
Single	15	2.9
Double	60/16.5	2.9/1.9
Triple	62.5/29.5/17	2.3/1.7/1.7

Table 2. Engine operation parameters and injection timing.

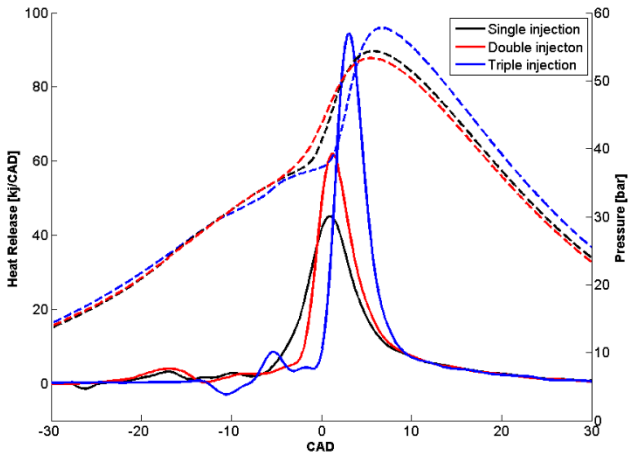

Figure 2. Rate of heat release (thick line) and pressure traces (dashed line) for different injection strategies.

In reference to PIV measurements, Figure 3 shows ensemble average flow fields measured at 12 CAD bTDC for different injection strategies. More detailed explanation on ensemble average flow fields are reported in a previous work [12].

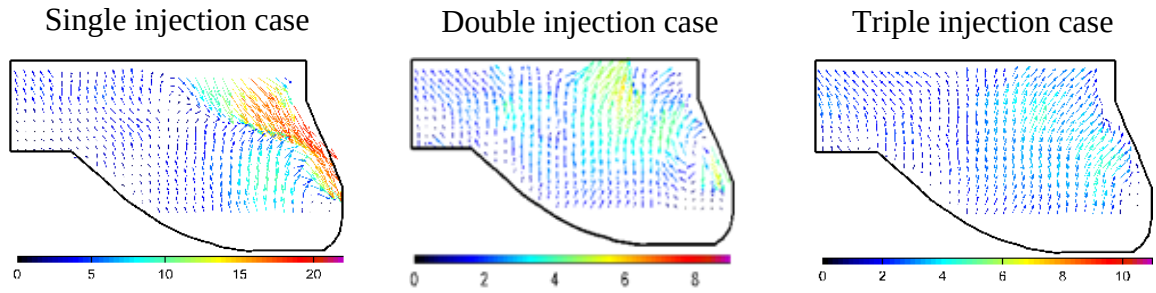

Figure 3. Ensemble Average velocity field in m/s at -12 CAD for single, double and triple injection.

3.2 Theoretical considerations

3.2.1 Turbulent Kinetic Energy calculation

Ensemble average velocity fields (coming from expressions such as Eq. (1)) are helpful to analyze the overall evolution of the flow field. In that expression, θ indicates the crank-angle and the index i refers to the cycle number (44 cycles for each crankshaft angular position). Nonetheless, the estimation of velocity fluctuations based on this approach is strongly influenced by cycle-to-cycle variations [10,12].

$$\bar{U}_{EA}(\theta) = \frac{1}{N}\sum_{i=1}^{N} \bar{U}(\theta, i) \tag{1}$$

To overcome this issue, flow field variations can be estimated within a temporal window. Following such approach, velocity field variations can be solved on a cycle-resolved basis. Consequently, for a given direction in the flow the cycle-resolved average can be solved at each pixel in the domain following Eq. (2):

$$\bar{U}(\theta, i) = \frac{1}{M}\sum_{j=1}^{M} C(j).U\left(\theta + \frac{2j - M - 1}{2}\Delta\theta\right) \tag{2}$$

The temporal window size is defined by the scalar M, which was set to five for this study i.e. the cycle-resolved average velocity field at TDC is a function of the instantaneous velocity fields measured at -4, -2, 0, 2 and 4 CAD. The variable Δθ is the temporal resolution of the measurements (2 CAD). Finally, the term $C(j)$ is a sine weight factor calculated according to Eq. (3):

$$C(j) = \frac{\sin\left(\frac{j}{M+1}\pi\right)}{\sum_{j=1}^{M}\sin\left(\frac{j}{M+1}\pi\right)} \tag{3}$$

Where: $\sum_{j=1}^{M} C(j) = 1$.

Once the cycle-resolved average field has been solved, the instantaneous fluctuations can be computed as the standard deviation within the temporal window following Eq. (4):

$$u'(\theta,i)=\sqrt{\frac{1}{M}\sum_{j=1}^{M}\left[U\left(\theta+\frac{2j-M-1}{2}\Delta\theta\right)-\bar{U}(\theta,i)\right]^2} \tag{4}$$

The instantaneous fluctuating components of velocity are then averaged over the total number of measurements (N is equal to the number of measured cycles) as expressed in Eq. (5):

$$\bar{u'}(\theta)=\frac{1}{N}\sum_{i=1}^{N}u'(\theta,i) \tag{5}$$

Lastly, the TKE associated to the fluctuations of velocity derived from PIV measurements is computed for every pixel in the domain using Eq. (6):

$$TKE(\theta)=\frac{1}{2}\left(\bar{u'}(\theta)^2+\bar{v'}(\theta)^2\right) \tag{6}$$

Based on the previous theoretical considerations, a particular methodology has been developed to comprehensively analyze spatial and temporal evolution of TKE. Figure 4 shows the TKE field at TDC under motored conditions. The contour of the bowl is marked with a solid black line. TKE is then averaged along the axial direction (marked with white dashed arrows). This averaged TKE is plotted at the bottom of the figure where 0 and 1 mark the bowl center and periphery, respectively. TKE has been normalized by the maximum value in the domain. This normalization allows for a more direct comparison of TKE spatial evolution under firing conditions.

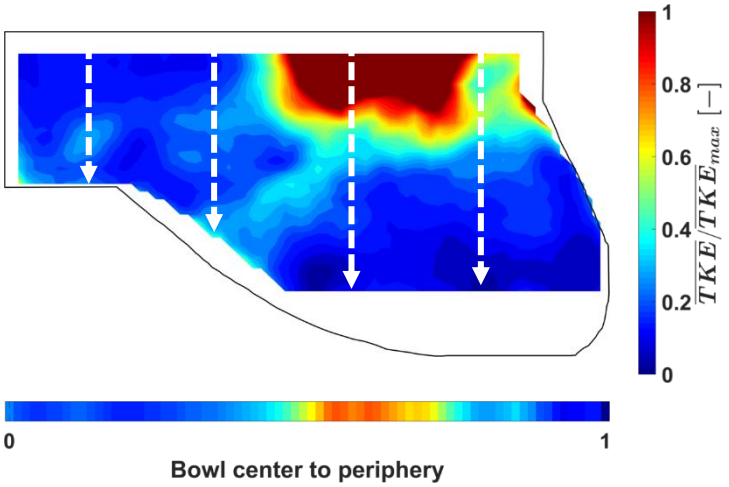

Figure 4. Normalized TKE at TDC under motored condition.

The same procedure described in Figure 4 is applied at all crank-angles at which PIV data is available. Normalized mean TKE plots are then rearranged as shown in Figure 5. Each column shows the spatial distribution of normalized TKE averaged over the axial direction. Then, on the right side of Figure 5 the temporal evolution of the maximum TKE value in the domain is also included. Under motored conditions, high TKE zones are located around the bowl middle area (between bowl center and periphery) as piston approaches TDC. In terms of magnitude, TKE maximum level also follows piston motion with increasing levels during late compression stroke. Once piston has reached TDC maximum levels decrease as expansion takes place with a moderate increase after 10 CAD aTDC (consistent with an increase in velocity magnitude, see Figure 6).

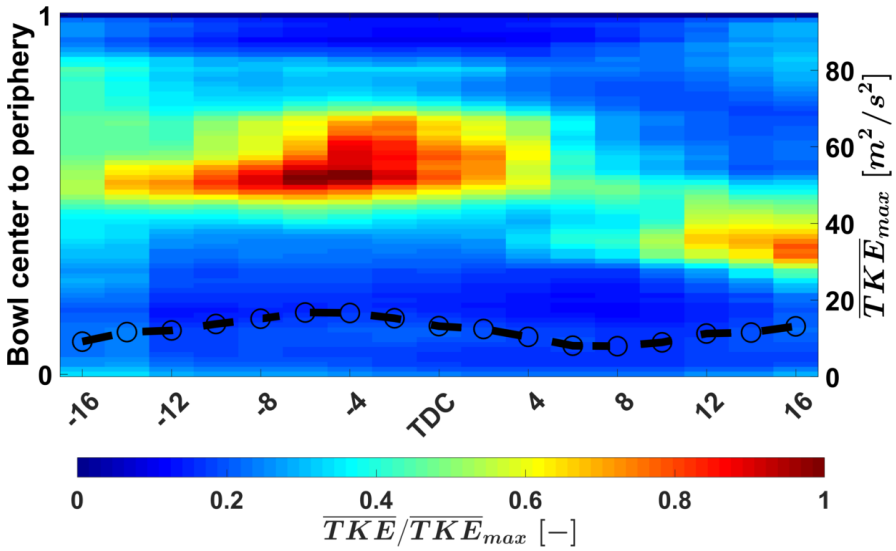

Figure 5. Normalized mean cycle-resolved TKE for motored condition case.

As in the case for TKE, velocity module has also been normalized and averaged in order to analyze the overall spatial and temporal evolution of the velocity field. Figure 6 shows the normalized mean ensemble average velocity module along with a plot (dashed black line) of the maximum value at each crank-angle. In this regard, maximum velocity values does not change significantly. In terms of spatial distribution, highest velocities take place at 16 CAD bTDC predominantly around bowl middle zone and periphery. Towards TDC, airflow decelerates at bowl periphery with predominant high velocities near bowl center. Throughout early expansion module of velocity starts raising again with dominant high velocity at bowl periphery.

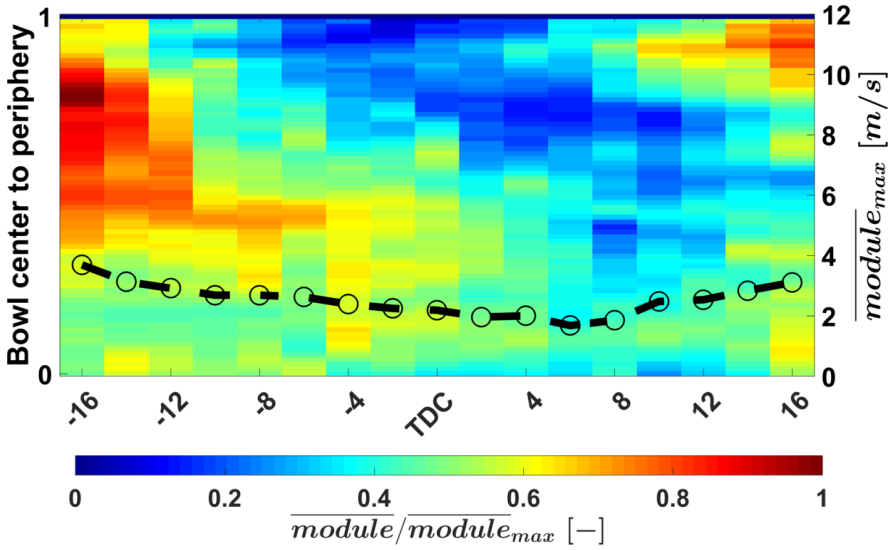

Figure 6. Normalized mean ensemble average velocity module for motored condition case.

3.3 1D model for tangential velocity estimation

It has been stated in the previous section that the PIV setup used allows to measure the in-cylinder radial (V) and axial (U) components of velocity. Nonetheless, if the flow flied is to be fully characterized the tangential component of velocity (swirl velocity) should be also studied. In that sense, the average evolution of this component is predicted by means of a 1D model [24]. The model is developed under the assumption that the in-cylinder volume can be divided into two zones as shown in Figure 7. Zone 1 considers the volume inside and above piston bowl meanwhile zone 2 considers the annular volume above piston bowl. It is also assumed that charge inside these volumes follows a solid-body rotation movement. Based on these statements, evolution of tangential velocity can be obtained resolving the change of angular momentum over time. This change can be solved for both volumes in terms of the increase and decrease of momentum flux. Increase of momentum flux is considered to be caused by mass flow coming into the volumes and momentum exchange between them due to squish flow and viscous shear forces. On the other hand, decrease of momentum flux is modeled by wall friction losses and mass flow going out of the volumes. The theoretical model has been validated with experimental PIV data measured in a horizontal section in an optical engine. The optical engine used as reference to validate 1D model predictions is a single-cylinder LD CI optical diesel engine. Engine displacement is 544.8 cm^3 with a cylindrical bowl. For validation, engine was operated under motored conditions and PIV measurements were carried out from 10 CAD bTDC up to 20 CAD aTDC with a 10 CAD temporal resolution.

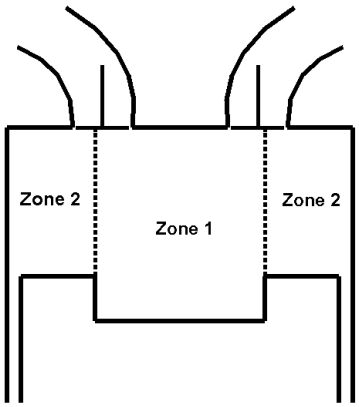

Figure 7. In-cylinder volumes used in the 1D model for tangential velocity prediction.

Solid line in Figure 8 shows the time evolution of tangential velocity (zone 1) predicted by the 1D model. Meanwhile, prediction of tangential velocity for the reference engine is plotted with a dashed line. Predicted values show proper agreement with experimental data marked with squares. For both cases, the increase in tangential velocity as piston approaches TDC is an expected trend. During compression, mass flow is confined inside the bowl inducing an increase in tangential velocity. Differences in tangential velocity between reference engine and the engine used for the current work are mainly caused by differences in cylinder head and intake port geometry as well as operating conditions.

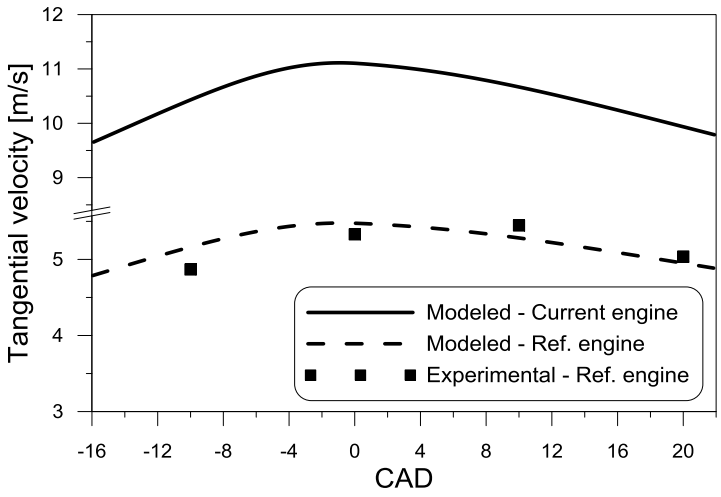

Figure 8. Tangential velocity evolution predicted by the 1D model.

3.4 Experimental wall heat transfer coefficient calculation

Based on the flow field characterization described in the previous sections an estimation of the convective wall heat transfer coefficient can be achieved. For that purpose, a variation of Woschni's approach [25] is used following Eq. (7)

$$h(\theta) = 0.012.D^{-0.2}.p(\theta)^{0.8}.T(\theta)^{-0.53}.V_c(\theta)^{0.8} \quad (7)$$

In the former expression, wall heat transfer coefficient can be estimated over time (θ makes reference to crank-angle) as a function of engine geometry (D is the bowl diameter), in-cylinder thermodynamic conditions assumed to be uniform (p and T are pressure and temperature, respectively) and the mean flow velocity. In the original empirical correlation presented by Woschni the mean flow velocity was assumed to be a function of piston mean velocity and the gas velocity that accounted for combustion influence. This approach introduces two additional constants that need to be fitted with experimental data. In this work the flow field influence on heat transfer coefficient is accounted by means of a characteristic velocity (V_c) as described in [24]. Although Woschni's empirical correlation is based on a global one-zone view of heat transfer it has been reported to be applicable for conventional diesel combustion as well as for low temperature combustion [26,27]. In the context of this work, Woschni's modified correlation is suitable to analyze trends and to study the influence of the injection pattern and the combustion process on the heat transfer coefficient. The aforementioned velocity is calculated following Eq. (8):

$$V_c(\theta) = \sqrt{V_{module}^2(\theta) + V_{tang}^2(\theta) + 2\overline{TKE}(\theta)} \quad (8)$$

Velocity module calculated with Eq. (9):

$$V_{module} = \sqrt{\bar{U}_{EA}{}^2 + \bar{V}_{EA}{}^2} \quad (9)$$

Magnitudes for V_{module} and $\overline{TKE}$ are derived from the PIV measurements and averaged over a layer with thickness equal to 5% of a characteristic length of the bowl (maximum radius of the bowl for this study) [28].

Experimentally derived magnitudes are functions of radial and axial components of velocity. On the other hand, V_{tang} is predicted by the 1D model previously described since the PIV setup used does not allow for this component of velocity to be measured. The use of this characteristic velocity leads to a more comprehensive estimation of wall heat transfer coefficient since flow field experimental data is used.

4 Results and discussion

4.1 Injection strategy effect on TKE

In this section, TKE spatial and temporal evolution is analyzed. The influence of injection and combustion events is studied for single and multiple injection strategies. Then, results from

the estimation of wall heat transfer temporal evolution are presented. At the end of the section, a comprehensive analysis of injection and combustion influence on TKE and wall heat transfer coefficient is made.

4.1.1 Single injection

TKE spatial and temporal evolution for the single injection strategy is presented in Figure 9. Dotted lines mark SOI (15 CAD bTDC) and EOI (12.1 CAD bTDC). In a similar way, dashed lines mark the combustion event at the crank-angle where 10% of the total heat release has been reached (CA10) and the crank-angle at which 90% of the total heat release has been reached (CA90). In addition, temporal evolution of the maximum TKE level in the domain is plotted on the right-side axis of the figure.

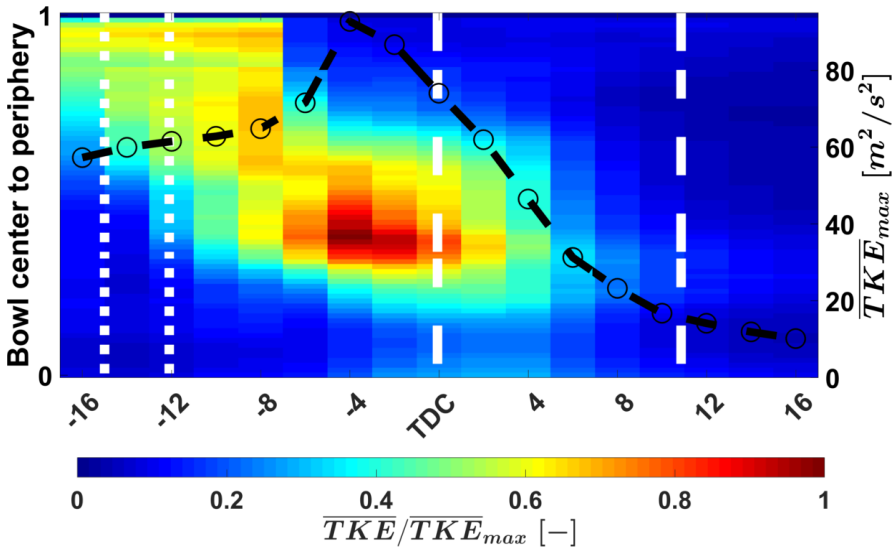

Figure 9. Normalized mean cycle-resolved TKE for single injection strategy.

In terms of spatial distribution, the injection event seems to induce high TKE levels especially near bowl periphery. This high TKE zones also seem to be broader up to 8 CAD bTDC. After this point, high TKE zones are located closer to bowl middle zone (between bowl center and periphery) as the squish flow becomes predominant. During the combustion process, the high TKE zone remains centered until it finally dissipates after 8 CAD aTDC. In terms of magnitude, injection event increases TKE level compared to the levels for motored case (see Figure 6). Additionally, squish flow seems to cause the peak value at the latest stage of the compression stroke. Concerning combustion, no TKE increase is introduced by this process. On the contrary, TKE keeps to continuously dissipate as far as 16 CAD aTDC.

Figure 10 shows a global view of how injection and combustion processes influence the flow field. As it was expected, before the start of the injection spatial distribution and maximum

value of velocity are consistent with results from the motored case. Once injection takes place, it is evident that this event strongly affects the flow field pattern. In terms of spatial distribution, the highest velocity level is reached around bowl periphery at 12 CAD bTDC. Beyond this point, moderate velocity levels are observed with the lowest levels taking place during expansion. Regarding temporal evolution of the maximum module of velocity (black dashed line), it can be seem that it is highly influenced by fuel injection with a sharp raise at the end of this event. Following fuel injection, maximum module of velocity increases and decreases alternatively at the same temporal range where high TKE levels were observed in Figure 9. In reference to combustion, after an initial raise of velocity around CA10 maximum velocity values drop to levels similar to the motored case levels.

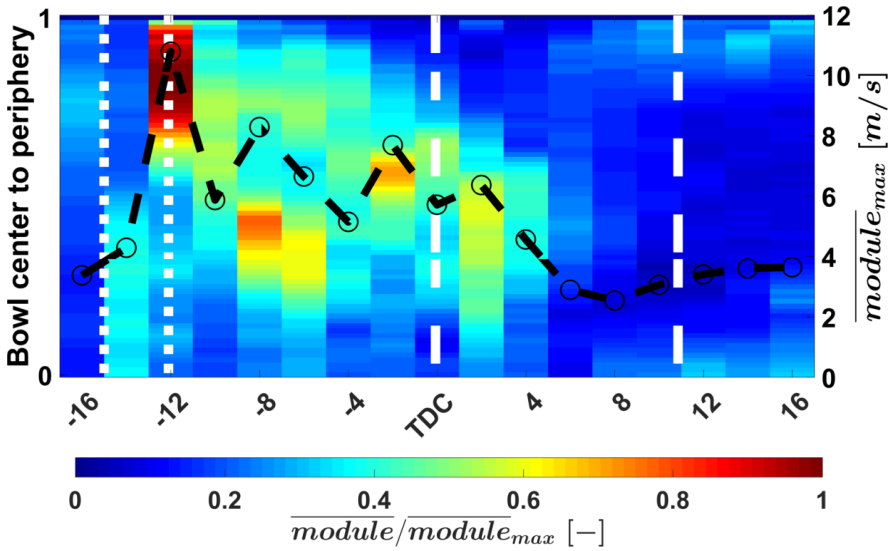

Figure 10. Normalized mean ensemble average velocity module for single injection strategy.

4.1.2 Double injection

The response of the in-cylinder TKE field to a double injection strategy was also evaluated. For that purpose, fuel was first injected at 60 CAD bTDC during 2.9 CAD with a second injection at 16.5 CAD with a 1.9 CAD duration (1 CAD shorter than the one for the single injection strategy). SOI and EOI of the last fuel injection are marked with dotted lines in Figure 11. On the other hand, dashed lines mark CA10 and CA90 for the combustion event.

Globally, TKE spatial distribution follows a close trend compared to the one observed with a single injection. The highest TKE levels are located at bowl periphery with more moderate levels towards bowl center. Such distribution remains unchanged as far as 8 CAD bTDC. This last observation differs from what was observed when a single fuel injection occurred. For that case, height of the moderate TKE zone only increased as piston approached TDC. This behavior is mainly related with the fact that with a single injection pattern, no TKE inducing

event takes place before fuel injection. On the other hand, in the double injection strategy TKE induced by the early injection at 60 CAD bTDC still seems to contribute to reach moderate TKE levels closer to bowl center. As for combustion, high TKE levels are reached in the middle area after CA10 and dissipate beyond 8 CAD aTDC with a moderate increase near bowl center at 16 CAD aTDC. Finally, the black dashed line shows that the highest TKE level in the domain does not change drastically over time following a smooth evolution independent from injection and combustion events.

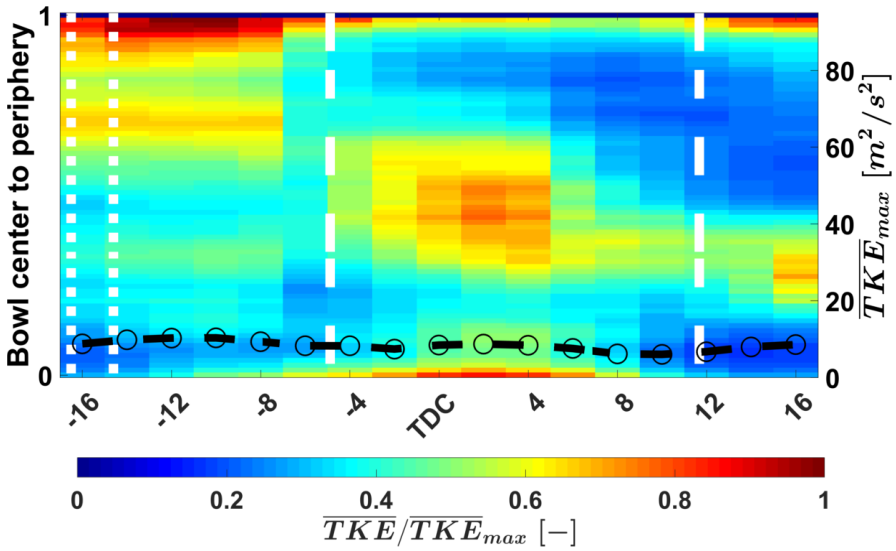

Figure 11. Spatial and temporal evolution of TKE for double injection strategy.

Normalized mean velocity module is shown in Figure 12. In this case, the second injection does not seem to heavily influence flow field contrary to what was observed for the single injection pattern. Spatially, velocity levels are more uniformly distributed up to CA10. During combustion, higher velocities take place closer to bowl center. In terms of magnitude, levels and temporal evolution are similar to results from the motored case.

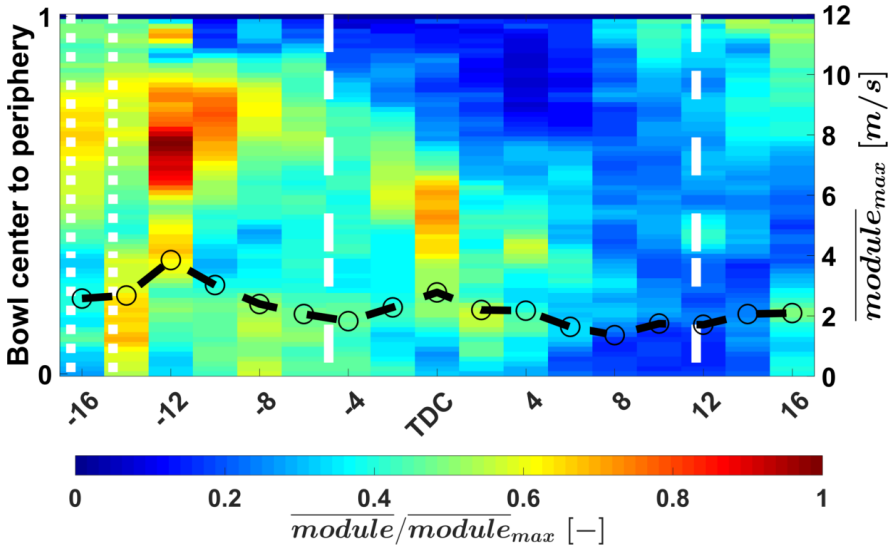

Figure 12. Normalized mean ensemble average velocity module for double injection strategy.

4.1.3 Triple injection

As part of the multiple injection approach, a triple injection strategy was also assessed. First and second injection start as early as 62.5 and 29.5 CAD bTDC with a duration of 2.3 and 1.7 CAD, respectively. The third injection also has a duration of 1.7 CAD with SOI and EOI marked with dotted lines in Figure 13. Similarly, combustion process is marked at CA10 and CA90 with dashed lines.

Injection and combustion events clearly are major contributors to the TKE field. In this matter, injection events predominantly introduce high TKE zones at bowl periphery (narrow red zone) at 16 CAD bTDC. At this same crank-angle, some moderate levels of TKE (mostly contributions from previous injections) can be observed. As compression progresses, TKE dissipates up to the point where combustion becomes predominant. After CA10, it promotes high TKE zones in the middle area of the domain with moderate levels evenly distributed throughout the rest of the bowl. After 6 CAD aTDC TKE starts to dissipate from bowl periphery towards its center up to 16 CAD aTDC. Under this injection strategy, the temporal evolution of the maximum TKE level (black dashed line) shows smooth raises at timings where injection and combustion dominates the flow.

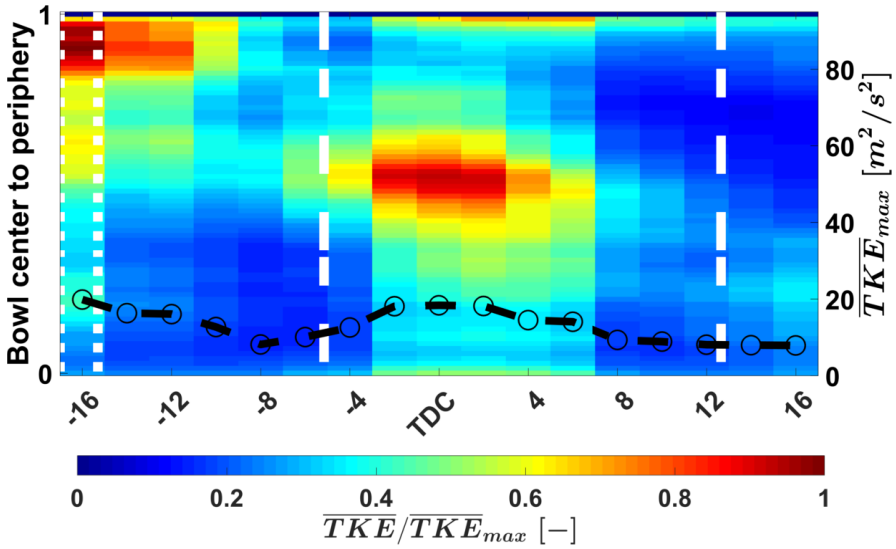

386 *Figure 13. Spatial and temporal evolution of TKE for triple injection strategy.*

387 In a similar way (in reference to double injection), the flow field under the triple injection
388 pattern achieves a more evenly distributed velocity field compare to the single injection
389 pattern. In Figure 14, it is seen that the third injection introduces high velocity levels around
390 bowl periphery followed by moderate velocity levels uniformly distributed in the domain up
391 to CA10. During early stages of combustion, higher velocities take place near bowl center
392 contrary to what is observed between 4 CAD aTDC and CA90. In terms of magnitude,
393 maximum velocity levels drop after the third injection and slightly increase beyond 8 CAD
394 aTDC, as seem for all cases.

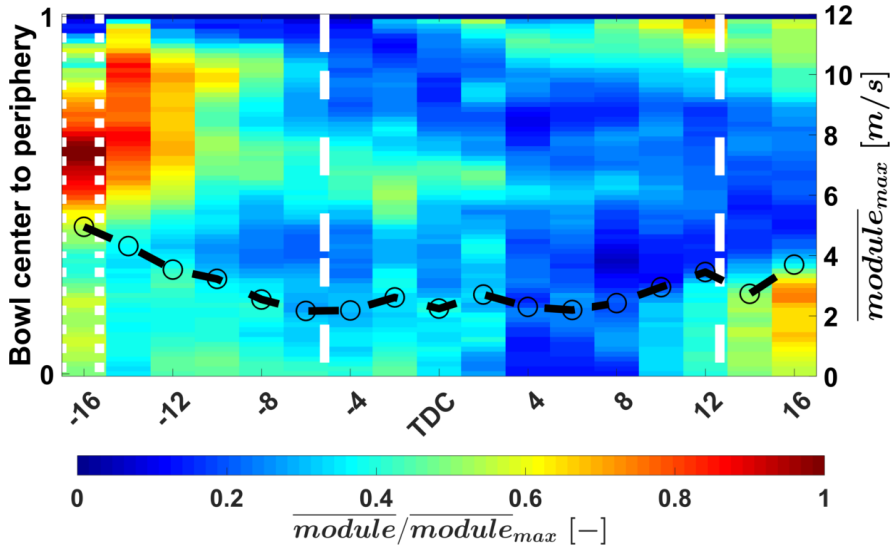

395 *Figure 14. Normalized mean ensemble average velocity module for triple injection strategy.*

396 **4.2 Wall heat transfer coefficient temporal evolution**

397 A modified Woschni's empirical correlation has been used to estimate how wall heat transfer
398 coefficient changes over time. As stated under the theoretical considerations section of this

work, the modified approach leads to a more comprehensive analysis since experimentally derived flow field parameters are taken into account. Figure 15 shows the temporal evolution of wall heat transfer coefficient for the motored case as well as for the firing cases. The injection pulse signal (arbitrary units) has also been plotted as reference. The injection pulse for the single injection pattern is plotted with a blue rectangle. Meanwhile, the injection pulse for the last injection in the double and triple injection patterns are plotted with red and black rectangles, respectively. It is evident that wall heat transfer coefficient temporal evolution highly depend upon injection pattern and consequently on combustion. To gain insight into how flow field interacts with fuel injection and combustion and how this interaction influences wall heat transfer coefficient, an analysis is made based on the methodology developed around TKE spatial and temporal evolution. The analysis is made in terms of how the different injection strategies introduce changes into the TKE field and how it differs from the motored case.

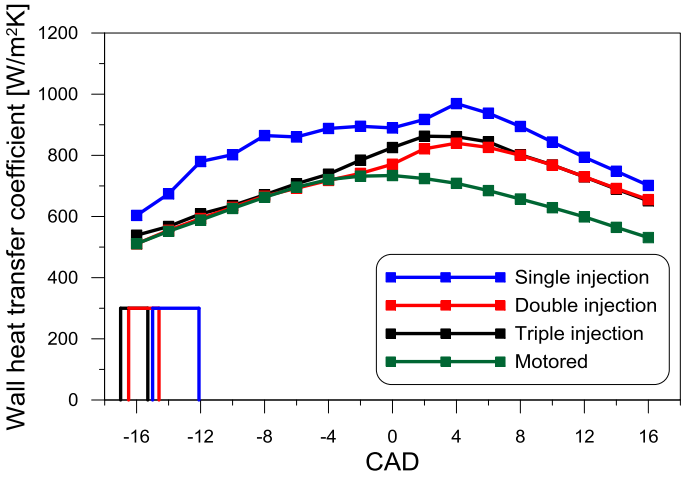

Figure 15. Wall heat transfer coefficient temporal evolution.

Figure 16 (from top to bottom) show in-cylinder pressure, temperature and characteristic velocity. These three magnitudes are the main terms driving wall heat transfer according to Eq. (7). For the single injection pattern, in-cylinder thermodynamic conditions does not differ from the motored case. Nonetheless, the characteristic velocity strongly differs from the motored case influenced by the injection event. Based on these observations, differences in wall heat transfer coefficient for the single injection pattern (in reference to the motored case) are not only driven by combustion (as it was expected), but also for the injection event that strongly influences the flow field. As for the multiple injection patterns, in-cylinder thermodynamic conditions remain close to the motored case before the start of combustion. Unlike the single injection pattern, in these cases the characteristic velocity does not strongly

differs from the motored case showing a less strong influence of injection on the flow field. As a result, wall heat transfer coefficient match the values from the motored case up to the start of combustion after which changes are mainly driven by thermodynamic conditions.

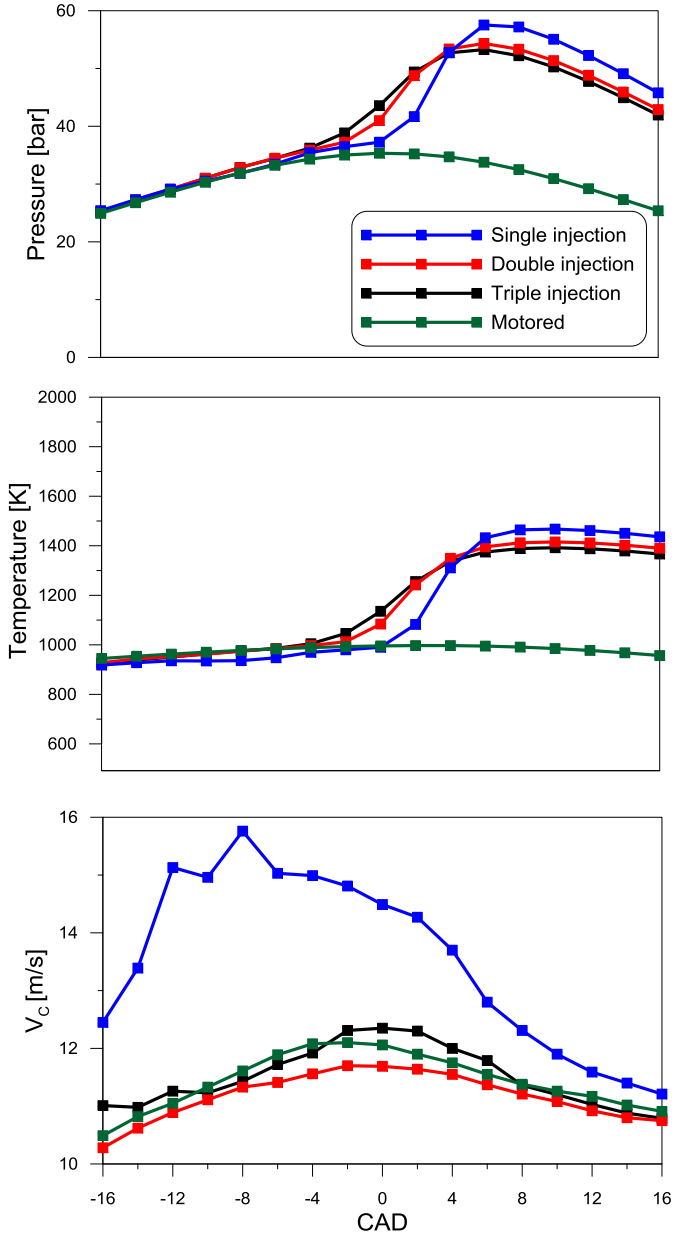

Figure 16. In-cylinder pressure, temperature and characteristic velocity for motored case and three different injection patterns.

To better understand influence of injection and combustion on the flow field (and hence on wall heat transfer coefficient), TKE fields for the different injection patterns have been normalized by subtracting the motored case TKE field. This normalization isolates contributions of injection and combustion allowing for a more suitable comparison. As in the previously presented TKE fields, in Figure 17 dotted lines are drown at SOI and EOI. Similarly, dashed lines mark CA10 and CA90 for combustion. For every injection pattern,

wall heat transfer coefficient differences respect to motored case are plotted with black dashed lines.

Fuel injection for the single injection pattern seems to cause TKE production at bowl periphery (see top part in Figure 17) up to EOI. Beyond that point, squish induced TKE seems to become predominant at bowl middle zone. Initial stages of combustion after CA10 introduce some differences that are quickly dissipated in the entire domain at crank-angles beyond 6 CAD aTDC.

As for multiple injection patterns, second injection under the double injection strategy introduces higher TKE levels at bowl periphery compared to motored condition as it was expected. Nonetheless, at bowl middle zone influence of squish is weaker under this injection pattern compared to motored condition (blue area). As previously observed for the single injection case, combustion predominantly influence the TKE field from bowl middle zone towards its center.

Once more, the last injection under the triple injection pattern promotes higher TKE levels (compared to motored condition) at bowl periphery. Although, unlike double injection, this third injection event seems to induce similar TKE levels compared to those reached under motored condition. As a result, the blue zone observed at bowl middle zone in the TKE field for double injection is smaller and weaker (in terms of intensity) in the TKE field for triple injection (bottom of the figure). Regarding combustion, it mainly influences bowl middle zone towards its center. However, under this injection pattern combustion also introduces high TKE levels around bowl periphery (narrow red zones). As in the other two injection patterns, TKE is dissipated beyond 6 CAD aTDC.

Finally, it is evident that wall heat transfer coefficient temporal evolution is strongly influenced by injection pattern. Black dashed lines show wall heat transfer coefficient differences respect to motored case. Top of Figure 17 shows how the single injection case differs the most respect to the reference case. Both injection and combustion processes induce sharp raises. It is noticeable that after EOI wall heat transfer coefficient remains close to the same level reached at EOI. However, during combustion peak level at 4 CAD aTDC is followed by a continuous drop.

For multiple injection cases, contrary to what was observed for the single injection pattern, wall heat transfer coefficient temporal evolution follows the motored case to a greater extend. After the last injection event, and up to CA10, the triple injection pattern seems to differ more

if compared to the double injection pattern. It is consistent with greater differences in TKE levels previously described. As for combustion, just after CA10 wall heat transfer coefficient for the triple injection pattern shows a slightly sharper increase respect to the double injection. However, longer combustions (multiple injection cases) come with wall heat transfer coefficient smoother temporal evolutions and lower peak values compared to the single injection case.

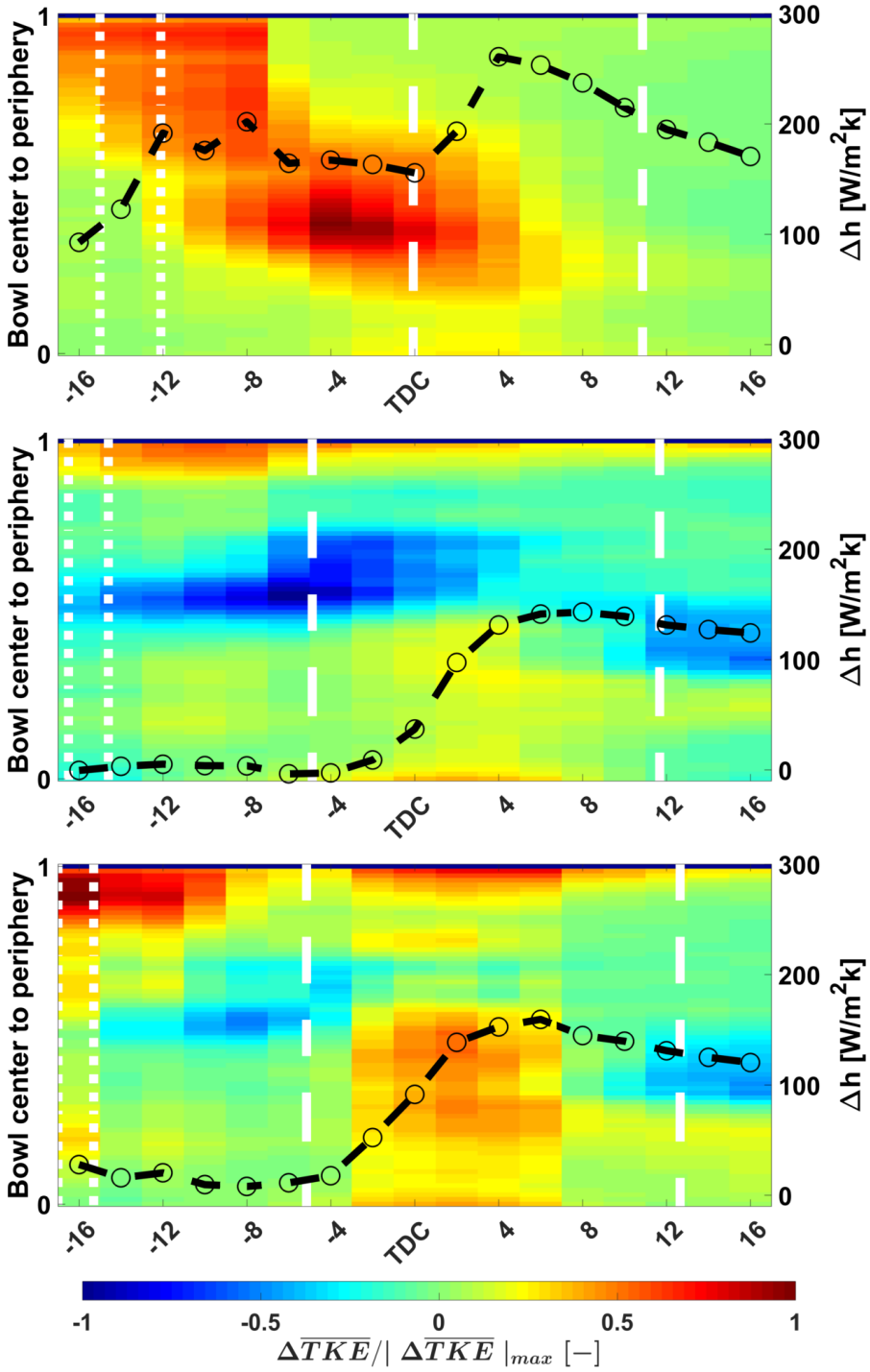

Figure 17. Overall spatial and temporal evolution of TKE difference between injection strategies and motored case. From top to bottom, single, double and triple injection.

5 Conclusions

Influence of spatial and temporal evolution of TKE on wall heat transfer coefficient has been studied. TKE has been computed based on PIV data measured in a vertical plane inside the combustion chamber of an optical engine with real bowl geometry. A methodology has been developed to represent maps with TKE temporal and spatial evolution. Wall heat transfer coefficient has also been computed based on a modification of the empirical correlation proposed by Woschni. Finally, results for several fuel injection strategies have been compared against the result from a reference case under motored conditions. Main remarks can be summarized as follows:

- Under motored conditions, piston movement seems to modulate TKE with peak levels towards TDC and around upper bowl area induced by squish flow stronger influence.
- Injection events introduce high TKE levels at bowl periphery. On the other hand, during combustion, high TKE levels take place at bowl middle zone.
- The single injection pattern introduces the greatest differences in the TKE field (in reference to motored case) compared to differences introduced by multiple injection patterns.
- For the single injection pattern, differences in wall heat transfer coefficient (in reference to motored case) before the start of combustion are mainly driven by changes in the flow field. After the start of combustion, differences in in-cylinder thermodynamic conditions also contribute to reach higher wall heat transfer coefficient levels than in the motored condition case.
- For multiple injection patterns, the greatest differences in wall heat transfer (in reference to motored case) take place after the start of combustion and are mainly driven by changes in the in-cylinder thermodynamic conditions since no significant changes are observed in the characteristic velocity.

Acknowledgements

The authors gratefully acknowledge the Swedish Energy Agency and the Competence Center for Combustion Processes KCFP. The authors also would like to acknowledge that part of the work has been partially funded by the Spanish government under the grant ‘‘José Castillejo” (JC2015/0036). Research leading to this work has also receive funding from Universitat Politècnica de València through the FPI program.

References

[1] M. Christensen, B. Johansson, The Effect of Combustion Chamber Geometry on HCCI Operation, Sae Tech. Pap. Ser. 2002 (2002). doi:10.4271/2002-01-0425.

[2] R. Hasegawa, H. Yanagihara, HCCI Combustion in DI Diesel Engine, SAE Tech. Pap. (2003). doi:10.4271/2003-01-0745.

[3] J.E. Dec, W. Hwang, M. Sjöberg, An Investigation of Thermal Stratification in HCCI Engines Using Chemiluminescence Imaging, (2006). doi:10.4271/2006-01-1518.

[4] V. Manente, B. Johansson, W. Cannella, Gasoline partially premixed combustion, the future of internal combustion engines?, Int. J. Engine Res. 12 (2011) 194–208.

[5] V. Manente, Gasoline Partially Premixed Combustion An Advanced Internal Combustion Engine Concept Aimed to High Efficiency, Low Emissions and Low Acoustic Noise in the Whole Load Range, Lund University, 2010.

[6] J. Benajes, S. Molina, A. García, E. Belarte, M. Vanvolsem, An investigation on RCCI combustion in a heavy duty diesel engine using in-cylinder blending of diesel and gasoline fuels, Appl. Therm. Eng. 63 (2014) 66–76. doi:10.1016/j.applthermaleng.2013.10.052.

[7] J. Benajes, A. García, J. Monsalve-Serrano, V. Boronat, Gaseous emissions and particle size distribution of dual-mode dual-fuel diesel-gasoline concept from low to full load, Appl. Therm. Eng. 120 (2017) 138–149. doi:10.1016/j.applthermaleng.2017.04.005.

[8] J. Benajes, A. García, J.M. Pastor, J. Monsalve-Serrano, Effects of piston bowl geometry on reactivity controlled compression ignition heat transfer and combustion losses at different engine loads, Energy. 98 (2016) 64–77. doi:10.1016/j.energy.2016.01.014.

[9] A.H. Kakaee, A. Nasiri-Toosi, B. Partovi, A. Paykani, Effects of piston bowl geometry on combustion and emissions characteristics of a natural gas/diesel RCCI engine, Appl. Therm. Eng. 102 (2016) 1462–1472. doi:10.1016/j.applthermaleng.2016.03.162.

[10] M. Izadi Najafabadi, S. Tanov, H. Wang, B. Somers, B. Johansson, N. Dam, Effects of Injection Timing on Fluid Flow Characteristics of Partially Premixed Combustion Based on High-Speed Particle Image Velocimetry, SAE Int. J. Engines. 10 (2017).

538 doi:10.4271/2017-01-0744.

539 [11] S. Lee, R.D. Reitz, Spray Targeting to Minimize Soot and CO Formation in Premixed
540 Charge Compression Ignition (PCCI) Combustion with a HSDI Diesel Engine, SAE
541 World Congr. 2006 (2006). doi:10.4271/2006-01-0918.

542 [12] S. Tanov, Z. Wang, H. Wang, M. Richter, B. Johansson, Effects of Injection Strategies
543 on Fluid Flow and Turbulence in Partially Premixed Combustion (PPC) in a Light
544 Duty Engine, SAE Tech. Pap. (2015). doi:10.4271/2015-24-2455.

545 [13] V. Manente, B. Johansson, P. Tunestal, M. Sonder, S. Serra, Gasoline partially
546 premixed combustion: high efficiency, low NOx and low soot by using an advanced
547 combustion strategy and a compression ignition engine, Int. J. Veh. Des. 59 (2012)
548 108–128. doi:10.1504/IJVD.2012.048689.

549 [14] G. Kalghatgi, L. Hildingsson, B. Johansson, Low NOx and low smoke operation of a
550 diesel engine using gasolinelike fuels, J. Eng. Gas Turbines Power. 132 (2010) 92803.

551 [15] M. Sellnau, M. Foster, K. Hoyer, W. Moore, J. Sinnamon, H. Husted, Development of
552 a Gasoline Direct Injection Compression Ignition (GDCI) Engine, SAE Int. J. Engines.
553 7 (2014) 835–851. doi:10.4271/2014-01-1300.

554 [16] M. Sellnau, W. Moore, J. Sinnamon, K. Hoyer, M. Foster, H. Husted, GDCI Multi-
555 Cylinder Engine for High Fuel Efficiency and Low Emissions, SAE Int. J. Engines. 8
556 (2015) 775–790. doi:10.4271/2015-01-0834.

557 [17] M. Sellnau, J. Sinnamon, K. Hoyer, H. Husted, Gasoline Direct Injection Compression
558 Ignition (GDCI) - Diesel-like Efficiency with Low CO2 Emissions, (2011).
559 doi:10.4271/2011-01-1386.

560 [18] Z. Wang, S. Tanov, H. Wang, M. Richter, B. Johansson, M. Alden, High-Speed
561 Particle Image Velocimetry Measurement of Partially Premixed Combustion (PPC) in a
562 Light Duty Engine for Different Injection Strategies, (2015). doi:10.4271/2015-24-
563 2454.

564 [19] H. Fridriksson, B.S. aen, S. Hajireza, M.T. aer, CFD Investigation of Heat Transfer in a
565 Diesel Engine with Diesel and PPC Combustion Modes, SAE Pap. 2011-01–18 (2011).
566 doi:10.4271/2011-01-1838.

567 [20] A. Broatch, P. Olmeda, A. García, J. Salvador-Iborra, A. Warey, Impact of swirl on in-

cylinder heat transfer in a light-duty diesel engine, Energy. (2016) 1–14. doi:10.1016/j.energy.2016.11.040.

[21] B. Petersen, P. Miles, PIV Measurements in the Swirl-Plane of a Motored Light-Duty Diesel Engine, SAE Int. J. Engines. 4 (2011) 1623–1641. doi:10.4271/2011-01-1285.

[22] K. Kiger, Introduction of Particle Image Velocimetry, (2010) 57. http://www2.cscamm.umd.edu/programs/trb10/presentations/PIV.pdf.

[23] J. Westerweel, Fundamentals of digital particle image velocimetry, Meas. Sci. Technol. 8 (1997) 1379–1392. doi:10.1088/0957-0233/8/12/002.

[24] C. Schubert, A. Wimmer, F. Chmela, Advanced Heat Transfer Model for CI Engines, SAE Tech. Pap. 2005 (2005). doi:10.4271/2005-01-0695.

[25] G. Woschni, A Universally Applicable Equation for the Instantaneous Heat Transfer Coefficient in the Internal Combustion Engine, SAE Int. (1967) 19. doi:10.4271/670931.

[26] F. Payri, X. Margot, A. Gil, J. Martin, Computational Study of Heat Transfer to the Walls of a DI Diesel Engine, SAE Tech. Pap. 2005 (2005). doi:10.4271/2005-01-0210.

[27] J. Chang, O. Güralp, Z. Filipi, D.N. Assanis, T.-W. Kuo, P. Najt, R. Rask, New Heat Transfer Correlation for an HCCI Engine Derived from Measurements of Instantaneous Surface Heat Flux, (2004). doi:10.4271/2004-01-2996.

[28] T. Morel, P. Blumberg, E. Fort, R. Keribar, Methods for heat analysis and temperature field analysis of the insulated diesel, NASA CR-174783,(DOE/NASA/0342-1). (1984).

Abbreviations

CA50: Crank Angle at 50% mass fraction burned

CA90: Crank Angle at 90% mass fraction burned

CAD: Crank Angle Degree

CI: Compression Ignition

EA: Ensemble average

EOI: End of Injection

h: Wall heat transfer coefficient

HCCI: Homogenous Charge Compression Ignition

LTC: Low Temperature Combustion

NOx: Nitrogen Oxides

PIV: Particle Image Velocimetry

PPC: Partially Premixed Combustion

RCCI: Reactivity Controlled Compression Ignition

SI: Spark Ignition

SOC: Start of Combustion

SOI: Start of Injection

TDC: Top Dead Center

TKE: Turbulent Kinetic Energy

V_c: Characteristic velocity

V_{module}: Module of velocity in the vertical plane

V_{tang}: Tangential component of velocity